Inorg. Chem. **2005**, *44*, 1290−1301

Determination of the g-Tensors and Their Orientations for *cis*,*trans*-(L-N_2S_2)$Mo^{V}OX$ (X = Cl, SCH_2Ph) by Single-Crystal EPR Spectroscopy and Molecular Orbital Calculations

Michele Mader Cosper,[†] Frank Neese,*[,‡] Andrei V. Astashkin,[†] Michael D. Carducci,[†] Arnold M. Raitsimring,[†] and John H. Enemark*[,†]

Department of Chemistry, University of Arizona, Tucson, Arizona 85721-0041, and Max-Planck-Institut für Bioanorganische Chemie, P.O. Box 101365, D-45413 Mülheim an der Ruhr, Germany

Received November 16, 2004

A single-crystal study of *cis*,*trans*-(L-N_2S_2)$Mo^{V}OCl$ (**1**) doped into *cis*,*trans*-(N_2S_2)$Mo^{VI}O_2$ (**3**) has enabled the **g**-tensor of **1** and its orientation with respect to the molecular structure to be determined. The EPR parameters (g_1, 2.004; g_2, 1.960; g_3, 1.946; A_1, 71.7×10^{-4} cm^{-1}; A_2, 11.7×10^{-4} cm^{-1}; A_3, 32.0×10^{-4} cm^{-1}) of *cis*,*trans*-(L-N_2S_2)Mo^{V}-OCl [L-$N_2S_2H_2$ = *N*,*N*′-dimethyl-*N*,*N*′-bis(mercaptophenyl)ethylenediamine] mimic those of the low-pH form of sulfite oxidase and the "very rapid" species of xanthine oxidase. The principal axis that corresponds to g_1 is rotated ∼10° from the Mo≡O vector, while the principal axis that corresponds to g_3 is located in the equatorial plane and ∼38° from the Mo−Cl vector. Independent theoretical calculations of the **g**-tensor of **1** were performed using two types of techniques: (1) the spectroscopically parametrized intermediate neglect of differential overlap technique (INDO/S) combined with single-excitation configuration interaction (CIS); (2) a scalar relativistic DFT (BP86 and B3LYP functionals) treatment using the zeroth order regular approximation to relativistic effects (ZORA) in combination with recently developed accurate multicenter mean field spin−orbit operators (RI-SOMF) and the estimation of solvent effects using dielectric continuum theory at the conductor-like screening model (COSMO) level. The excellent agreement between experiment and theory, as well as the high consistency between the INDO/S and BP86/ZORA results, provides a sound basis for analysis of the calculated orientation of the **g**-tensor for *cis*,*trans*-(L-N_2S_2)$Mo^{V}O(SCH_2Ph)$ (**2**), for which single-crystal EPR data are not available but which contains three equatorial sulfur donor atoms, as occurs in sulfite oxidase and xanthine oxidase. The implications of these results for the EPR spectra of the Mo(V) centers of enzymes are discussed.

Introduction

Molybdenum is associated with more than 40 enzymes that catalyze two-electron oxidation−reduction reactions that are of crucial importance in the metabolism of C, N, and S by all forms of life.[1,2] These enzymes have been classified into three families[1,3] on the basis of the coordination about the molybdenum atom, as revealed by X-ray absorption spectroscopy (XAS)[4−8] and recent X-ray crystal structures,[9,10] and their amino acid sequences.[11] Sulfite oxidase (SO) has been shown to contain a $[Mo^{VI}O_2]^{2+}$ core in its fully oxidized state.[12] The coordination sphere of the five-coordinate, square

* Authors to whom correspondence should be addressed. E-mail: jenemark@u.arizona.edu (J.H.E.); neese@mpi-muelheim.mpg.de (F.N.). Fax: 520 626-8065 (J.H.E.); +49-208-306-3951 (F.N.).
[†] University of Arizona.
[‡] Max-Planck-Institut für Bioanorganische Chemie.

(1) Hille, R. *Chem. Rev.* **1996**, *96*, 2757−2816.
(2) Sigel, A.; Sigel, H. *Molybdenum and Tungsten: Their Roles in Biological Processes*; Metals Ions in Biological Systems Vol. 39; Dekker: New York, 2002.
(3) Hille, R. In *Metals Ions in Biological Systems*; Sigel, A., Sigel, H., Eds.; Dekker: New York, 2002; pp 187−226.
(4) Hille, R.; George, G. N.; Eidsness, M. K.; Cramer, S. *Inorg. Chem.* **1989**, *28*, 4018−4022.
(5) George, G. N.; Prince, R. C.; Mukund, S.; Adams, M. W. W. *J. Am. Chem. Soc.* **1992**, *114*, 3521−3523.
(6) George, G. N.; Garrett, R. M.; Prince, R. C.; Rajagopalan, K. V. *J. Am. Chem. Soc.* **1996**, *118*, 8588−8592.
(7) Baugh, P. E.; Garner, C. D.; Charnock, J. M.; Collison, D.; Davies, E. S.; McAlpine A. S.; Bailey, S.; Lanes, I.; Hanson, G. R.; McEwan, A. G. *J. Biol. Inorg. Chem.* **1997**, *2*, 634−643.
(8) George, G. N.; Hilton, J.; Temple, C.; Prince, R. C.; Rajagopalan, K. V. *J. Am. Chem. Soc.* **1999**, *121*, 1256−1266.
(9) Dobbeck, H.; Huber, R. In *Metals Ions in Biological Systems*; Sigel, A., Sigel, H., Eds.; Dekker: New York, 2002, pp 228−263.
(10) Kisker, C. *Handbook of Metalloproteins*; Messerschmidt, A., Huber, R., Poulos, T., Wieghardt, K., Eds.; John Wiley & Sons Ltd.: New York, 2001; Vol. 2, pp 1121−1135.

10.1021/ic0483850 CCC: $30.25
Published on Web 02/15/2005

pyramidal Mo center is completed[13] by three thiolate S atoms in equatorial positions, one from a cysteine side chain and the other two from the pyranopterindithiolate[14,15] (molybdopterin)[16,17] found in all molybdoenzymes. It has been postulated that the "very rapid" signal exhibited by xanthine oxidase (XO) results from a $Mo^{V}OS_3$ coordination site containing two S atoms from the pyranopterindithiolate ligand and one S atom from a terminal sulfido ligand.[4,18−25]

During enzymatic turnover, the Mo centers of SO and XO are proposed to shuttle through the $Mo^{IV}/Mo^{V}/Mo^{VI}$ oxidation states.[1,26−29] CW-EPR spectroscopy has been used to determine the **g**- and **A**(^{95}Mo)-tensors of the Mo(V) centers of mononuclear Mo enzymes[20,21,30−32] and many model compounds.[20,21,33−43] Due to the random orientation of the paramagnetic molecules in the frozen solution samples, the orientation of the **g**- and **A**-tensors relative to the molecular structure cannot be determined by solution CW-EPR spectroscopy. For crystalline synthetic Mo(V) compounds, the relatively small distances between individual molecules in the solid state usually result in extensive dipolar broadening of the EPR signals that precludes accurate determination of the **g**- and **A**-tensors. Experimental determination of the orientations of the **g**- and **A**-tensors relative to the molecular structure requires magnetically dilute single crystals. The Mo centers of enzymes are well-separated because of the large sizes of the protein molecules; however, to date no Mo-containing enzyme has been prepared in a crystalline form *with a suitable concentration of the Mo(V) state* to allow direct experimental determination of the orientations of the **g**- and **A**-tensors in the molecular coordinate frame. Only a limited number of Mo(V) compounds have been studied by dilute single-crystal EPR methods[44−53] because of the major difficulty in preparing a suitable diamagnetic host compound.

The paramagnetic compounds studied here include *cis,trans*-(L-N_2S_2)$Mo^{V}OCl$ (**1**) and *cis,trans*-(L-N_2S_2)$Mo^{V}O(SCH_2$-Ph) (**2**) [where L-$N_2S_2H_2$ = *N*,*N*′-dimethyl-*N*,*N*′-bis(mercaptophenyl)ethylenediamine]. The structural characteristics and the EPR parameters of **1**[54] and **2**[43] (Table 1) show similarities to the *lpH* and *hpH* forms of SO[30,31] and the "very rapid" species of XO.[19] Compound **2** contains a $Mo^{V}OS_3$ core, where all the Mo−S bonds reside in the equatorial plane cis to the apical Mo≡O bond,[43] as occurs in SO.[13] Even though **2** does not possess an ene−dithiolate moiety, the relative orientations of the pπ orbitals of two of the adjacent S atoms mimic those of an ene−1,2-dithiolate (Figure 1).[37,43] The EPR parameters for **2** are remarkably similar to those of the *lpH* form of SO[30,31] and the "very rapid" form of XO (Table 1).[19,20] Despite extensive synthetic efforts,[52] it has not yet been possible to synthesize a diamagnetic host for **2** for experimental determination of the orientations of its **g**- and **A**(^{95}Mo)-tensors. Therefore, the understanding of the relationship of the EPR parameters of **2** to molecular structure relies heavily on the *independent* theoretical analysis that is

(11) Kisker, C.; Schindelin, H.; Rees, D. C. *Annu. Rev. Biochem.* **1997**, *66*, 233−267.
(12) George, G. N.; Pickering, I. J.; Kisker, C. *Inorg. Chem.* **1999**, *38* (10), 2539−2540.
(13) Kisker, C.; Schindelin, H.; Pacheco, A.; Wehbi, W. A.; Garrett, R. M.; Rajagopalan, K. V.; Enemark, J. H.; Rees, D. C. *Cell* **1997**, *91*, 973−983.
(14) Hille, R. *JBIC, J. Biol. Inorg. Chem.* **1997**, *2*, 804−809.
(15) Fischer, B.; Enemark, J. H.; Basu, P. *J. Inorg. Biochem.* **1998**, *72*, 13-21.
(16) Rajagopalan, K. *Enzymol. Relat. Areas Mol. Biol.* **1991**, *64*, 215−289.
(17) Rajagopalan, K. V.; Johnson, J. L. *J. Biol. Chem.* **1992**, *267*, 10199−10202.
(18) Cramer, S. P.; Hille, R. *J. Am. Chem. Soc.* **1985**, *107*, 8164−8169.
(19) George, G. N.; Bray, R. C. *Biochemistry* **1988**, *27*, 3603−3609.
(20) Wilson, G. L.; Greenwood, R. J.; Pilbrow, J. R.; Spence, J. T.; Wedd, A. G. *J. Am. Chem. Soc.* **1991**, *113*, 6803−6812.
(21) Greenwood, R. J.; Wilson, G. L.; Pilbrow, J. R.; Wedd, A. G. *J. Am. Chem. Soc.* **1993**, *115*, 5385−5392.
(22) Romão, M. J.; Archer, M.; Moura, J. J. G.; LeGall, J.; Engh, R.; Schneider, M.; Hof, P.; Huber, R. *Science* **1995**, *270*, 1170−11776.
(23) Huber, R.; Hof, P.; Duarter, R. O.; Moura, J. J. G.; Moura, I.; Liu, M.; LeGall, J.; Hille, R.; Archer, M.; Romão, M. *Proc. Natl. Acad. Sci. U.S.A.* **1996**, *93*, 8846−8851.
(24) Enroth, C.; Eger, B. T.; Okamoto, K.; Nishino, T.; Nishino, T.; Pai, E. F. *Proc. Natl. Acad. Sci. U.S.A.* **2000**, *97*, 10723−10728.
(25) Truglio, J. J.; Theis, K.; Leimkuhler, S.; Rappa, R.; Rajagopalan, K.; Kisker, C. *Structure* **2002**, *10*, 115−125.
(26) Rajagopalan, K. *Molybdenum and Molybdenum Containing Enzymes*; Coughlan, M., Ed.; Pergamon: Oxford, U.K., 1980; pp 241−272.
(27) Brody, M. S.; Hille, R. *Biochemistry* **1999**, *38*, 6668−6677.
(28) Pacheco, A.; Hazzard, J. T.; Tollin, G.; Enemark, J. H. *JBIC, J. Biol. Inorg. Chem.* **1999**, *4*, 390−401.
(29) Astashkin, A. V.; Mader, M. L.; Pacheco, A.; Enemark, J. H.; Raitsimring, A. M. *J. Am. Chem. Soc.* **2000**, *122*, 5294−5302.
(30) Dhawan, I. K.; Pacheco, A.; Enemark, J. H. *J. Am. Chem. Soc.* **1994**, *116*, 7911−7912.
(31) Dhawan, I. K.; Enemark, J. H. *Inorg. Chem.* **1996**, *35*, 4873−4882.
(32) Bray, R. C. In *Biological Magnetic Resonance*; Reuben, J., Berliner, L. J., Eds.; Plenum Press: New York, 1980; pp 45−84.
(33) Collison, D.; Mabbs, F. E.; Enemark, J. H.; Cleland, W. E., Jr. *Polyhedron* **1986**, *5*, 423−425.
(34) Guiles, R. D. M.S. Thesis, San Francisco State University, San Francisco, CA, 1983.
(35) Dowerah, D.; Spence, J. T.; Singh, R.; Wedd, A. G.; Wilson, G. L.; Farchione, F.; Enemark, J. H.; Kristofski, J.; Bruck, M. *J. Am. Chem. Soc.* **1987**, *109*, 5655−5665.
(36) Enemark, J. H.; Young, C. G. *Adv. Inorg. Chem.* **1993**, *40*, 1−88.
(37) Peariso, K.; Chohan, B. S.; Carrano, C. J.; Kirk, M. L. *Inorg. Chem.* **2003**, *42*, 6194−6203.
(38) Chang, C. S. J.; Enemark, J. H. *Inorg. Chem.* **1991**, *30*, 683−688.
(39) Chang, C. S. J.; Collison, D.; Mabbs, F. E.; Enemark, J. H. *Inorg. Chem.* **1990**, *29*, 2261−2267.
(40) Chang, C. S. J.; Pecci, T. J.; Carducci, M. D.; Enemark, J. H. *Inorg. Chem.* **1993**, *32*, 4106−4110.
(41) Cleland, W. E., Jr.; Barnhart, K. M.; Yamanouchi, K.; Collison, D.; Mabbs, F. E.; Ortega, R. B.; Enemark, J. H. *Inorg. Chem.* **1987**, *26*, 1017−1025.
(42) Lim, B. S.; Willer, M. W.; Maio, M.; Holm, R. H. *J. Am. Chem. Soc.* **2001**, *123*, 8343−8349.
(43) Mader, M. L.; Carducci, M. D.; Enemark, J. H. *Inorg. Chem.* **2000**, *39*, 525−531.
(44) Garner, C. D.; Hill, L. H.; Mabbs, F. E.; McFadden, D. L.; McPhail, A. T. *J. Chem. Soc., Dalton Trans.* **1977**, 853−858.
(45) Collison, D.; Eardley, D. R.; Mabbs, F. E.; Rigby, K.; Enemark, J. H. *Polyhedron* **1989**, *8*, 1833−1834.
(46) Garner, C. D.; Lambert, P.; Mabbs, F. E.; King, T. J. *J. Chem. Soc., Dalton Trans.* **1977**, 1191−1198.
(47) Garner, C. D.; Howlander, N. C.; Mabbs, F. E.; Boorman, P. M.; King, T. J. *J. Chem. Soc., Dalton Trans.* **1978**, 1350−1354.
(48) Gahan, B.; Howlander, N. C.; Mabbs, F. E. *J. Chem. Soc., Dalton Trans.* **1981**, 142−149.
(49) Collison, D.; Eardley, D. R.; Mabbs, F. E.; Rigby, K.; Bruck, M. A.; Enemark, J. H.; Wexler, P. A. *J. Chem. Soc., Dalton Trans.* **1994**, 1003−1011.
(50) Balagopalakrishna, C.; Kimbrough, J. T.; Westmoreland, T. D. *Inorg. Chem.* **1996**, *35*, 7758−7768.
(51) Nipales, N. S.; Westmoreland, T. D. *Inorg. Chem.* **1997**, *36*, 756−757.
(52) Mader, M. L. Ph.D. Dissertation, University of Arizona, Tucson, AZ, 2000.
(53) Mabbs, F. E.; Collison, D. *Electron Paramagnetic Resonance of d Transition Metal Compounds*; Elsevier Science: Amsterdam, 1992.
(54) Barnard, K. R.; Bruck, M.; Huber, S.; Grittini, C.; Enemark, J. H., Gable; Wedd, A. G. *Inorg. Chem.* **1997**, *36*, 637−649.

Table 1. EPR Data for Chicken Liver Sulfite Oxidase, Xanthine Oxidase, and Oxo−Mo(V) Complexes with Sulfur Donor Ligands

signal	g_1[a]	g_2	g_3	$\langle g \rangle$	A_1[b]	A_2	A_3	$\langle A \rangle$	α[c]	b	g
SO (low pH form)[d]	2.007	1.974	1.968	1.983	56.7	25.0	16.7	32.8	0	18	0
SO (high pH form)[d]	1.990	1.966	1.954	1.970	54.4	21.0	11.3	28.9	0	14	22
XO (very rapid, xanthine)[e]	2.025	1.955	1.949	1.977	44.4	18.2	19.1	27.2	8	36	0
XO (rapid, type 1, formamide)[e]	1.990	1.971	1.967	1.976	61.4	24.7	25.7	37.3	0	18	0
XO (type 2)[f]	1.990	1.968	1.962	1.973	60.4	24.7	24.8	36.6	0	20	0
XO (slow)[f]	1.971	1.966	1.954	1.964	65.4	26.2	27.1	39.6	0	33	0
cis,*trans*-(L-N_2S_2)$Mo^{V}OCl$ (**1**)[g]	2.004	1.960	1.946	1.970	71.7	11.7	32.0	38.5	0	31[h]	0
cis,*trans*-(L-N_2S_2)$Mo^{V}O(SCH_2Ph)$ (**2**)[i]	2.022	1.963	1.956	1.980	58.4	23.7	22.3	34.8	0	24	0
$[Mo^{V}OCl(SC_6H_2$-2,4,6-$Pr^{i}_3)(bdt)]^{-}$[j]	2.017	1.978	1.963	1.986	58	12	39	36			
(L3S)MoO(bdt)[k]	2.016	1.972	1.949	1.979	52	26	24	34	8	40	0

[a] Error ±0.001. [b] $A(^{95,97}Mo)$, $\times 10^{-4}$ cm^{-1}; errors $\pm 1 \times 10^{-4}$ cm^{-1}. [c] Errors ±2°. [d] References 30 and 31. [e] Reference 19. [f] Reference 21. [g] Reference 54. [h] Rotation about g_3. [i] Reference 43. [j] Reference 42. [k] Reference 37.

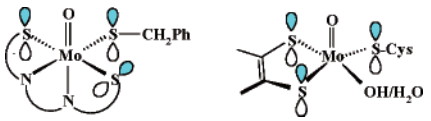

Figure 1. Left: Schematic view of the structure of **2**.[43] The cis, trans geometry of the tetradentate L-N_2S_2 ligand constrains one Sπ orbital to be in the equatorial plane; the remaining two Sπ orbitals are cis to one another, approximately perpendicular to the equatorial plane and parallel to the Mo≡O bond. Right: Active site of SO[13] with all three Sπ orbitals approximately perpendicular to the equatorial plane and parallel to the Mo≡O bond.

presented here. The calculations on **2** are validated by parallel studies on compound **1**[54] for which single-crystal EPR data have been obtained. The six-coordinate Mo(V) center of *cis*,*trans*-(L-N_2S_2)$Mo^{V}OCl$ (**1**) possesses two thiolate S donors that are trans to one another.[54] Crystals of **1** are isomorphous with diamagnetic *cis*,*trans*-(L-N_2S_2)$Mo^{VI}O_2$[35,54] (**3**), which is an excellent host lattice for single-crystal EPR studies of **1**. Thus, compound **1** provides a low-symmetry compound with sulfur coordination for independently determining the relationship between the **g**- and **A**-tensors and the molecular structure by experiment and by theory.

Compound **2** and congeners with other monodentate thiolates[43,54] were the *first* synthetic analogues of the SO site with three thiolate donors in the equatorial plane. Subsequently, Holm and co-workers prepared several five-coordinate Mo(V,VI) complexes that contain benzene-1,2-dithiolate (bdt) and a monodentate thiolate in the equatorial plane and whose EPR and metric parameters closely mimic those of SO.[42,55] Very recently the structure and spectroscopic properties of a six-coordinate oxo−Mo(V) compound with equatorial coordination including bdt and a sterically constrained monodentate thiolate have been described (Table 1).[37]

Insight into the electronic origin of the observed **g**-tensor and its orientation for a given paramagnet can be obtained by electronic structure calculations.[56,57] Previously an intermediate neglect of differential overlap (INDO/S) methodology was presented and applied to Mo(V) centers by Peng et al.[58] More recently Westmoreland et al.[50,59] used a simple connection from DFT to ligand field theory to discuss **g**-tensors and hyperfine couplings of Mo(V) model complexes in relation to single-crystal EPR measurements. In recent years, several methods have become available to calculate **g**-tensors more rigorously from DFT.[60−65] However, until recently, the DFT methods had not progressed to the stage where they give quantitative agreement with experiment. Therefore, for the bulk of this work, we have utilized the INDO/S methodology combined with single-excitation configuration interaction (INDO/S-CIS) developed earlier.[66,67] This method is readily applied to large systems and has proven its ability to give a balanced description of the electronic states of a wide variety of transition metal complexes, including those of Mo.[58] For this study, the close agreement between the experimental and theoretical results for the **g**-tensor of **1** provides a firm foundation for using the same theoretical framework for calculating the electronic structure and interpreting the **g**-tensor of **2**, a low-symmetry oxo−Mo(V) compound whose coordination environment more closely mimics that of molybdoenzymes but for which single-crystal EPR data are not available. In addition to the experimentally calibrated semiempirical results, we also report some pilot scalar relativistic DFT calculations of EPR **g**-tensors and hyperfine couplings. These methods are rather new and have so far not been applied in practical calculations. (For reviews on DFT approaches to EPR parameters, see refs 56, 57, and 68) Here, we provide a first test of their accuracy and also use them to validate the semiempirical results.

Experimental Section

Materials. Unless otherwise stated, all manipulations were performed under an inert atmosphere with dried and deaerated

(55) Jalilehvand, F.; Lim, B. S.; Holm, R. H.; Hedman, B.; Hodgson, K. O. *Inorg. Chem.* **2003**, 42, 5531−5536.
(56) Neese, F. *Curr. Opin. Chem. Biol.* **2003**, *7*, 125.
(57) Neese, F.; Solomon, E. In *Magnetoscience-From Molecules to Materials*; Miller, J. S., Drillon, M., Eds.; Wiley: New York, 2003; pp 345−466.
(58) Peng, G.; Nichols, J.; McCullough, E. A.; Spence, J. *Inorg. Chem.* **1994**, *33*, 2857−2864.
(59) Swann, J.; Westmoreland, T. D. *Inorg. Chem.* **1997**, *36*, 5348−5357.
(60) Schreckenbach, G.; Ziegler, T. *J. Phys. Chem. A* **1997**, *101*, 3388−3399.
(61) Malkina, O. L.; Vaara, J.; Schimmelpfennig, B.; Munzarová, M.; Malkin, V. G.; Kaupp, M. *J. Am. Chem. Soc.* **2000**, *122*, 9206−9218.
(62) Kaupp, M.; Reviakine, R.; Malkina, O. L.; Arbuznikov, A.; Schimmelpfennig, B.; Malkin, V. G. *J. Comput. Chem.* **2002**, *23*, 794−803.
(63) Van Lenthe, E.; Wormer, P. E. S.; Van Der Avoird, A. *J. Chem. Phys.* **1997**, *107*, 2488−2498.
(64) Neyman, K. M.; Ganyushin, D. I.; Matveev, A. V. *J. Chem. Phys. A* **2002**, *106*, 5022−5030.
(65) Neese, F. *J. Chem. Phys.* **2001**, *115*, 11080−11096.
(66) Neese, F. *Int. J. Quantum Chem.* **2001**, *83*, 104−114.
(67) Neese, F.; Solomon, E. I. *Inorg. Chem.* **1998**, *37*, 6568−6582.
(68) Kaupp, M., Malkin, V., Bühl, M., Eds. *Calculation of NMR and EPR Parameters*, Wiley-VCH, 2004.

Table 2. Comparison of Unit Cells for Crystals of *cis,trans*-(L-N_2S_2)MoO_2{O,Cl}

	crysl 1	cryst 2
formula	$C_{16}H_{18}MoN_2O_2S_2$	$C_{16}H_{18}MoN_2O_2S_2$
color	dark green-yellow	dark orange-red
dimens (mm)	0.43 × 0.25 × 0.04	2.33 × 0.92 × 0.33
fw	430.39	430.39
temp, K	171	298
cryst system	monoclinic	monoclinic
a, Å	10.0363(9)	10.060(2)
b, Å	14.504(1)	14.524(2)
c, Å	12.044(1)	12.153(2)
β, deg	103.618(2)	103.69(1)
V, Å^3	1704.0(2)	1775.7
Z	4	4
space group	$P2_1/n$ (No. 14)	$P2_1/n$ (No. 14)

solvents. *cis,trans*-(L-N_2S_2)$Mo^{V}OCl$[54] (**1**) and *cis,trans*-(L-N_2S_2)-$Mo^{VI}O_2$[35] (**3**) were prepared according to previously published methods.

Crystal Structure Determination. An X-ray diffraction quality crystal (crystal 1) was prepared by layering pentane over a CH_2Cl_2 solution of **1** and **3** in a 3:97 ratio. A large single crystal (crystal 2) was obtained by layering pentane over a saturated CH_2Cl_2 solution containing **1** and **3** in a 1:99 ratio and seeded with several small single crystals of **3**.

Crystallographic data are given in Tables S1−S3 for crystal 1. The intensity data were collected on a Bruker AXS single-crystal diffractometer with a SMART 1000 CCD detector, using a Mo Kα radiation source with a graphite crystal monochromator. The intensity data were corrected for Lorentz and polarization effects. The data were integrated using the SAINT program,[69] and an empirical absorption correction using SADABS[70] was applied. The final unit cell was determined from 21 424 reflections derived from the full data set. All hydrogen atoms were constrained during refinement using the riding model. The structure was solved by direct methods using SIR-92,[71] and least-squares refinement (based on *F*) was performed using teXsan.[72]

A unit cell (Table 2) was determined for crystal 2, which was used for the single-crystal EPR experiment. A total of 20 frames were collected, and the faces were indexed using the Bruker SMART software.[73]

EPR Spectroscopy. Crystal 2, a large dark green plate with the crystallographic *b* axis normal to the plate face, was mounted on a two-axis goniometer[74] with epoxy. X-band CW-EPR spectra of the doped single crystal were recorded on a Bruker ESP 300 spectrometer. The EPR spectra were recorded at 5° increments over 360° in three orthogonal planes: the *ab*, *bc**, and *ac** crystallographic planes.[52]

Calculations. Molecular orbital (MO) calculations were carried out with the program ORCA2000[75] and the INDO/S model Hamiltonian of Zerner and co-workers[76,77] at the experimental geometries. The self-consistent field (SCF) calculations were of the restricted open-shell Hartree−Fock (ROHF) type.[78] The SCF calculations were followed by a configuration interaction (CI) procedure in the space of all spin symmetry-adapted single excitations. This procedure also includes the so-called trip-doublet excitations in which an electron is promoted from a doubly occupied MO *i* to an empty MO *a* followed by a spin flip in MO *a* to produce a triplet excitation and a concomitant spin flip in the ground-state SOMO orbital to produce an excited state with a correct total spin of $S = 1/2$. These excitations are important since they induce the spin-polarization effects into the ground-state wave function. In the CI calculation, all excitations within a 30 × 30 orbital window were considered, and the CI matrix was formed by a Rumer diagram technique.[79−81] The lowest 120 roots of the CI matrix were determined, and from the resulting many electron wave functions ($\Psi_0-\Psi_n$) and energies (E_0-E_n) the *g*-shifts were evaluated according to the following equation:

$$\Delta g_{pq} = -2\sum_b \Delta_b^{-1}\{\langle\Psi_0|\sum_i l_p(i)|\Psi_b\rangle\langle\Psi_b|\sum_{iA}\xi(r_{iA})l_{A,q}(i)s_z(i)|\Psi_0\rangle + \langle\Psi_0|\sum_{iA}\xi(r_{iA})l_{A,q}(i)s_z(i)|\Psi_b\rangle\langle\Psi_b|\sum_i l_p(i)|\Psi_0\rangle\} \quad (1)$$

Here Δ_b is the excitation energy from the ground state to the excited stated Ψ_b, $l_p(i)$ is the *p*th component of the angular momentum operator for electron *i*, $l_{A,q}(i)$ is the *q*th component of the angular momentum operator for electron *i* relative to atom *A*, $s_z(i)$ is the *z*-component of the spin-operator for electron *i* and Ψ_b, and $l_p(i)$ is the spin−orbit coupling operator for atom *A*. In the semiempirical approximation, the spin−orbit term is approximated using the valence shell spin−orbit coupling constants which were taken to be 25 cm^{-1} for C, 76 cm^{-1} for N, 150 cm^{-1} for O, 374 cm^{-1} for S, 695 cm^{-1} for Mo(4d), and 735 cm^{-1} for Mo(5p). Finally, from the diagonalization of the tensor $\mathbf{g}^{\mathbf{T}}\mathbf{g}$, the orientation of the **g**-tensor relative to the molecular axis system is determined.

In the final stages of this work, we have gained the ability to properly treat the relativistic effects on the structure, energetics, and EPR parameters of heavy-element compounds at the all-electron level. We therefore have reoptimized the structures of **1** and **2** using the zeroth-order regular approximation to relativistic effects (ZORA)[82] which we have implemented into the latest version of ORCA,[83] according to the model potential idea of van Wüllen.[84] The basis sets used were fully decontracted to allow for the accurate description of the distortion of the core orbitals brought about by the relativistic effects. For H and C the polarized split-valence basis of Schäfer et al. was used (SV(P)[85]), while N, O, and S were described by the more accurate polarized triple-ζ basis (TZVP[86,87]). The molybdenum center is most critical in this respect, and in this work we have chosen a "safe" approach and have used a very large,

(69) SAINT V. 5.01: *Software for the CCD Detector System*; Brucker Analytical X-ray System: Madison, WI, 1998.
(70) Blessing, R. H. SADABS: Program for absorption corrections using Seimens CCD based in the method of Robert Blessing. *Acta Crystallogr.* **1995**, *A51*, 33−38.
(71) Altomare, A.; Cascarano, M.; Giacovazzo, C.; Guagliardi, A. *J. Appl. Crystallogr.* **1993**, *26*, 343.
(72) *teXsan*: *Single-Crystal Structure Analysis Software*, V. 1.8; Molecular Structure Corp.: 3200 Research Forest Drive, The Woodlands, TX 77381, 1992, 1997.
(73) *SMART, Software for the Bruker AXS Single-Crystal Diffractometer*; Brucker Analytical X-ray System: Madison, WI, 1998.
(74) Morton, J. R.; Preston, K. F. *J. Magn. Reson.* **1983**, *52*, 457.
(75) Neese, F. Unpublished program, 2000.
(76) Ridley, J.; Zerner, M. *Theor. Chim. Acta* **1973**, *32*, 111−134.
(77) Zerner, M. C.; Loew, G. H.; Kirchner, R. F.; Mueller-Westerhoff, U. T. *J. Am. Chem. Soc.* **1980**, *102*, 589−599.
(78) Edwards, W. D.; Zerner, M. C. *Theor. Chim. Acta* **1987**, *72*, 347−361.
(79) Reeves, C. M. *Commun. ACM* **1966**, *9*, 276.
(80) Cooper, I. L.; McWeeny, R. *J. Chem. Phys.* **1966**, *45*, 226−234.
(81) Sutcliffe, B. T. *J. Chem. Phys.* **1966**, *45*, 235−239.
(82) van Lenthe, E.; Snijders, J. G.; Baerends, E. *J. Chem. Phys.* **1996**, *105*, 6505.
(83) Neese, F. *ORCA-an ab initio, Density Functional and Semiempirical Program Package*, version 2.4, revision 12; Max Planck Institut für Bioanorganische Chemie: Mülheim an der Ruhr, Germany, July 2004.
(84) van Wüllen, C. *J. Chem Phys.* **1998**, *109*, 392.
(85) Schäfer, A.; Horn, H.; Ahlrichs, R. *J. Chem. Phys.* **1992**, *97*, 2571.
(86) Schäfer, A.; Huber, C.; Ahlrichs, R. *J. Chem. Phys.* **1994**, *100*, 5829.
(87) Ahlrichs, R.; May, K. *Chem. Phys.* **2000**, *2*, 943.

uncontracted, well-tempered basis set of quality 28s20p17d[88,89] which gives close to basis set limit accuracy. While the large, uncontracted basis sets make the calculations somewhat costly, the high efficiency of the ORCA package still allows for the completion of these calculations within 1 day of computing time on single CPU personal computers. Accurate numerical integration was enforced in the presence of steep basis functions.[90] Structures were fully optimized in redundant internal coordinates[91] through an interface of ORCA to TurboMole.[92] For the geometry optimizations (but *not* the property calculations), only one-center ZORA corrections were considered. This eliminates the need for analytic gradients of the relativistic corrections and introduces negligible errors in the final structures.[93]

Hyperfine interactions were calculated at the optimized geometries according to van Lenthe's formulation within the ZORA formalism,[94] and spin−orbit effects were calculated as developed in ref 95. In this work, the recently developed multicenter mean-field SOC (RI-SOMF) operator was used,[96] which is based on the pioneering work of Hess et al.[97] and generalizes the already very successful[61] atomic mean field approach.[98] This operator explicitly takes care of the one- and two-electron parts of the Breit−Pauli SOC operator and includes the spin-same-orbit (SSO) as well as spin-other-orbit (SOO) terms in its two-electron part. In the **g**-tensor calculations, the same SOC operator was used, and the calculations were performed according to the coupled-perturbed Kohn−Sham formalism which expresses the **g**-tensor as a second-order response property with respect to homogeneous external magnetic field and spin−orbit-coupling perturbations.[99] Structures and properties were optimized with the BP86 functional.[100,101] Finally, we have studied the solvent effect on the computed properties within the conductor-like screening model (COSMO) of Klamt,[102] which was recently implemented into ORCA in an efficient way.[103]

Results and Discussion

Structural Characterization of *cis,trans*-(L-N_2S_2)MoO_2{O,Cl}. Unit cell parameters are given in Table S1 and Table 2; an ORTEP diagram of the magnetically dilute single crystals is shown in Figure 2. Positional parameters, anisotropic thermal parameters, and complete bond distances and bond angles are given in the Supporting Information (Tables S1−S10). The crystal used for the EPR measurements (crystal 2) had unit cell parameters (Table 2) similar to those of the one used for structure determination (crystal 1). The structural parameters determined for *cis,trans*-(L-N_2S_2)MoO_2{O,Cl} are only slightly different from those for pure crystals of **1** and **3**.[35,54] The small differences in the unit cell and structural parameters of *cis,trans*-(L-N_2S_2)MoO_2{O,Cl} arise from the partial occupation of the O4 and O5 sites of **3** by a Cl atom of **1.** Also, the larger ionic radius of a Cl atom results in a slightly larger unit cell and apparent elongation of the Mo1═O4 and Mo1═O5 bonds from 1.697 Å in **3** to 1.718 and 1.743 Å in *cis,trans*-(L-N_2S_2)MoO_2{O,Cl}. Thus, the structural parameters of the doped crystal closely resemble those of **3**. However, it is to be expected that the *cis,trans*-(L-N_2S_2)MoOCl molecules in the magnetically dilute crystal will exhibit 2-fold disorder, as occurs in pure crystals of **1**,[54] because the bulky L-N_2S_2 ligand dominates the crystal packing interactions. The two alternative forms of **1** have nearly identical coordination geometries about the Mo atom and differ primarily in the orientation of the MoOCl fragment, with the two possible Mo positions being separated by ∼0.75 Å (Figure S8).[54] Table S10 compares the coordination geometries of the two forms of **1** with **3**.

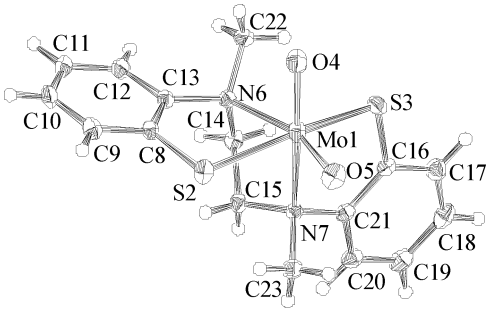

Figure 2. View of the structure and numbering scheme of *cis,trans*-(L-N_2S_2)MoO_2{O,Cl} determined for the crystal with **1** doped into **3** (see text). The Mo−O4 bond vector lies approximately parallel to the *c** axis. The structure shown for the doped crystal is not significantly different from that for pure **3**.[35]

Single-Crystal EPR Spectroscopy. *cis,trans*-(L-N_2S_2)-MoO_2{O,Cl} belongs to the space group $P2_1/n$ (*b* axis unique), and four molecules are contained in the monoclinic unit cell (Figure S1). The orthogonal coordinate frame consisted of the *c** axis and the mutually perpendicular *a* and *b* axes. The CW-EPR measurements were made for single-crystal orientations obtained by rotations in three orthogonal planes, *ab*, *ac**, and *bc** (Figures S2−S7). The *g*-values were determined, and g^2 was plotted as a function of the angle of rotation (Figure 3). In the space group $P2_1/n$, two molecules are related by an inversion center; a 2_1 rotation of this pair generates the second pair of molecules. Therefore, in the *ab* and *bc** planes, two signals should be observed, one from each magnetically distinguishable pair. However, four signals were observed in the *bc** plane (rotation about *a*, Figures 3, S2, and S3) because the Cl atom of **1** can occupy either the O4 or O5 site of **3**.[54] This disorder of the Cl atom over two sites effectively produces two different molecules of **1** per asymmetric unit and thereby doubles the number of signals observed in the *bc** plane. By the same reasoning, a total of four signals are also

(88) Huzinaga, S.; Miguel, B. *Chem. Phys. Lett.* **1990**, *175*, 289.
(89) Huzinaga, S.; Klobukowski, M. *Chem. Phys. Lett.* **1993**, *212*, 260.
(90) Neese, F. *Inorg. Chim. Acta* **2002**, *337C*, 181.
(91) von Armim, M.; Ahlrichs, R. *J. Chem. Phys.* **1999**, *111*, 9183.
(92) Ahlrichs, R.; Bär, M.; Baron, H.; Bauernschmitt, R.; Böcker, S.; Ehrig, M.; Eichkorn, K.; Elliott, S.; Furche, F.; Haase, F.; Häser, M.; Horn, H.; Huber, C.; Öhm, H.; Schäfer, A.; Schneider, U.; Treutler, O.; von Arnim, M.; Weigend, F.; Weis, P.; Weiss, H. *TURBOMOLE Program System for ab initio Electronic Structure Calculations, Version 5.2*; University of Karlsruhe: Karlsruhe, Germany, 2000.
(93) van Lenthe, J.; Fass, S.; Snijders, J. G. *Chem. Phys. Lett.* **2000**, *328*, 107.
(94) van Lenthe, E.; van der Avoird, A.; Wormer, E. *J. Chm. Phys.* **1998**, *108*, 4783.
(95) Neese, F. *J. Chem. Phys.* **2003**, *118*, 3939.
(96) Neese, F. *J. Chem. Phys.* **2005**, *122*, 34107.
(97) Hess, B.; Marian, C.; Wahlgren, U.; Gropen, O. *Chem. Phys. Lett.* **1996**, *251*, 365.
(98) Schimmelpfennig, B. *The Atomic Mean Field Spin−Orbit Coupling (AMFI) Program*; Stockholm University: Stockholm, Sweden, 1996.
(99) Neese, F. *J. Chem. Phys.* **2001**, *115*, 11080.
(100) Becke, A. *Phys. Rev. A.* **1988**, *38*, 3098.
(101) Perdew, J. *Phys. Rev. B.* **1986**, *33*, 8822.
(102) Klamt, A.; Schuurmann, G. *J. Chem. Soc., Perkin Trans.* **1993**, *2*, 799.
(103) Wennmohs, F.; Diedhenhofen, M.; Klamt, A.; Neese, F. Manuscript in preparation.

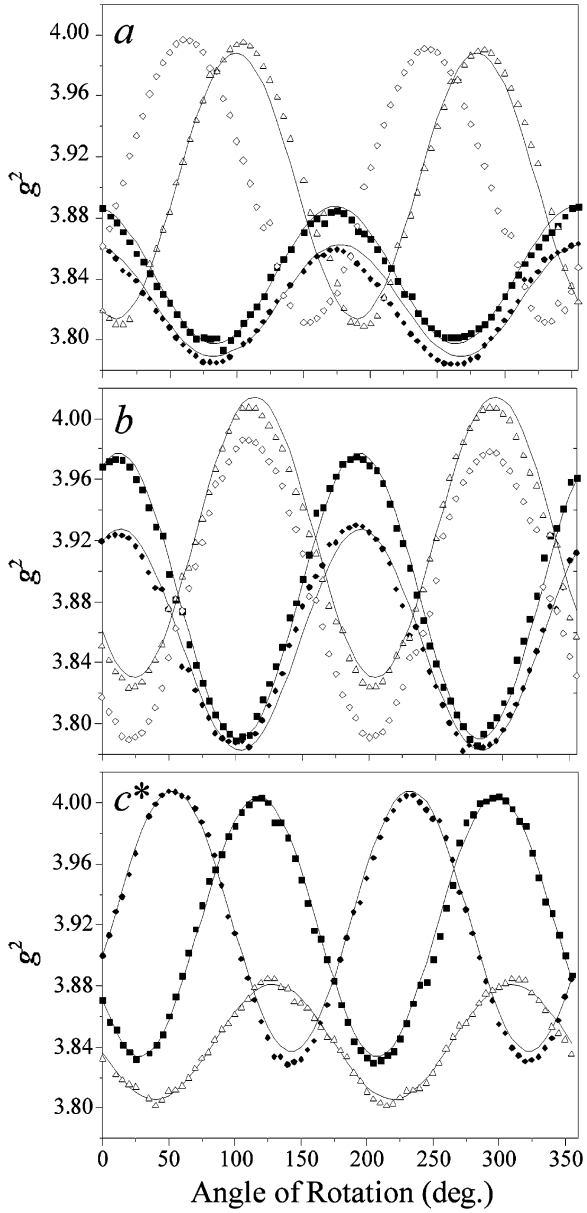

Figure 3. Plots of the variation of g^2 versus rotation for three mutually perpendicular planes: (top) rotation about *a* for observation of the *bc** plane; (middle) rotation about *b* for observation of the *ac** plane; (bottom) rotation about *c** for observation of the *ab* plane. The symbols ■, ●, Δ, and ◇ mark the experimental g^2 values observed for species 1−4, respectively. The best fits for species 1−3 are shown by solid lines. Species 4 could not be measured accurately for rotation about *c** (bottom).

expected for the*ab* plane (rotation about *c**); however, only three signals could be tracked in this rotation (Figures 3, S4, and S5).

In the *ac** plane, all four symmetry-related molecules in space group $P2_1/n$ are magnetically equivalent because the 2_1 screw axis is parallel to the *b* axis, and only two signals are expected due to the disorder of the Cl atom over the O4 and O5 sites. However, four signals were observed in the *ac** plane (rotation about *b*, Figures 3, S6, and S7). The additional pair of signals may be due to very slight misalignments of the two disordered sites of **1** relative to the diamagnetic host and/or to minor misalignments of the host crystal on the goniometer. In view of the known disorder,[54] more quantitative assessment of the possible misorientation[104] was not warranted.

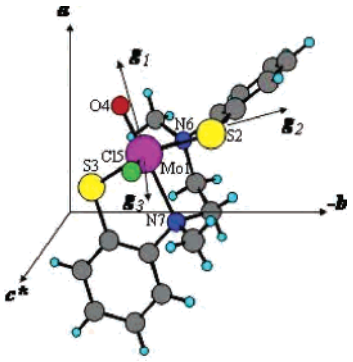

Figure 4. Relationships among the molecular structure, magnetic vectors (g_1, g_2, g_3), and crystallographic (*a*, *b*, *c**) axes for **1**. Substitution of O5 of **3** by Cl is shown, which corresponds to species 1 (■) of Figure 3.

Figure 4 shows one possible orientation of **1** relative to the crystal and molecular frames of the host lattice. The structure was obtained by replacing O5 of **3** by a chlorine atom. The structure of **1** in Figure 4 is not strictly correct, however, because the disorder of **1** does not result in exact coincidence Mo≡O and Mo−Cl bonds for the two contributors,[54] as discussed above and shown in Figure S8. Nonetheless, Figure 4 and the fractional coordinates of Table S4 show that the *c** direction is approximately parallel to Mo−O5 (or Mo−Cl5) and that the *a* axis is in the general direction of Mo−O4 (or Mo−Cl4). Thus, rotations about *a* or *c** both correspond qualitatively to rotations about the Mo−O and Mo−Cl bonds of the two disordered species (Figure 4) and consequently their plots (*bc** and *ab* planes, respectively, Figure 3) are similar to one another. Both of these plots exhibit two sets of traces, consistent with rotation about distinctly different bonds (Mo≡O or Mo−Cl) in the two disordered forms of **1**. The *b* axis is roughly perpendicular to the MoOCl plane (Figure 4), and rotation about *b* (*ac** plane) shows qualitatively similar curves, consistent with the various positions of the disordered MoOCl fragment being approximately parallel to the *ac** plane.

Relationship of the Molecular Structure to g_1, g_2, and g_3. The $\mathbf{g^Tg}$ matrixes can be extracted from the experimental data (Figure 3) by solving the following:[105]

$$g^2 = (\mathbf{g^Tg})_{aa}\sin^2\theta\cos^2\varphi + (\mathbf{g^Tg})_{ab}\sin^2\theta\sin 2\varphi + (\mathbf{g^Tg})_{bb}\sin^2\theta\sin^2\varphi + (\mathbf{g^Tg})_{ac}\sin 2\theta\cos\varphi + (\mathbf{g^Tg})_{bc}\sin 2\theta\sin\varphi + (\mathbf{g^Tg})_{cc}\cos^2\theta \quad (2)$$

Here θ and φ are respectively the polar and azimuthal angles of the magnetic field vector $\mathbf{B_o}$ in the (*a*, *b*, *c**) coordinate frame. The $\mathbf{g^Tg}$ matrixes of species 1 and 2 relative to the crystal frame are given in Table 3. Diagonalization of these $\mathbf{g^Tg}$ matrixes gives the magnitudes of the magnetic vectors (g_1, g_2, g_3) for each species and their angles with the crystallographic (*a*, *b*, *c**) axes (Table 4). The magnitudes

(104) Waller, W.; Rogers, M. *J. Magn. Reson.* **1973**, *9*, 92−107.
(105) Weil, J. A.; Bolton, J. R.; Wertz, J. E. *Electron Paramagnetic Resonance: Elementary Theory and Practical Applications*; John Wiley and Sons: New York, 1994.

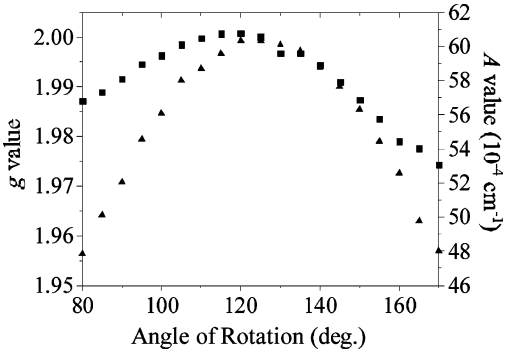

Figure 5. Plot of the maximum values of g and A (g_1 and A_1) versus the angle of rotation. The squares show g_1, and the triangles show A_1.

Table 3. $\mathbf{g}^T\mathbf{g}$ Matrixes in the Crystal Frame

	a	*b*	*c**
	Species 1 (■)		
a	3.972	0.0625	−0.034
b	0.0625	3.877	0.0135
*c**	−0.034	0.0135	3.800
	Species 2 (●)		
a	3.930	−0.0715	−0.032
b	−0.0715	3.877	−0.0025
*c**	−0.032	−0.0025	3.788

Table 4. Principal g-Values and the Angles (deg) between Principal Axes of the **g**-Tensors and Crystallographic Axes

	Species 1 (■)		
	2.001	1.964	1.946
a	26	70	74
b	65	32	71
*c**	83	66	25
	Species 2 (●)		
	1.996	1.958	1.943
a	35	61	72
b	56	37	76
*c**	83	69	23

of g_1, g_2, and g_3 were found to be within ±0.008 of the frozen solution g-values (Table 1).

The **A**(^{95}Mo) tensor could not be deconvoluted, but the CW-EPR spectra (Figures S2−S7) demonstrated that the largest component of this **A**-tensor increased and decreased in proportion to the largest component of the **g**-tensor (Figure 5). Therefore, the axis of the largest **A**-tensor component (A_1) must be nearly coincident with the axis of the largest **g**-tensor component. Since the largest **A**-tensor component is usually placed perpendicular to the plane of the orbital containing the unpaired electron, d_{xy},[44−46,48−53,106−108] the preferred solution for the orientation of g_1, g_2, and g_3 relative to the molecular structure of **1** is with g_1 and A_1 closest to the Mo≡O bond. The Cl atom of **1** can reside in either the O4 or O5 site of **3**. Replacing O5 by Cl results in a self-consistent set of angles between the g-axes and the molecular frame for species 1 (■) and 2 (●) that place g_1 (1.998) to be 10° from the Mo≡O4 vector, 78° from the Mo−Cl vector, and 84° from the Mo−S2 vector; g_3 (1.944) to be 38° from the Mo−Cl vector, 82° from the Mo≡O4 vector, and 54° from the Mo−S2 vector; and g_2 (1.961) at 37° from the Mo−S2 vector, 86° from the Mo≡O4 vector, and 54° from the Mo−Cl vector (Table 5). Thus, species 1 (■) and 2 (●) are assigned to structurally identical, but magnetically inequivalent, molecules that are related to one another by symmetry operations of the space group. An additional complication in determining the angles of Table 5 is that the disorder of **1** results in not only two different sets of Mo, O, and Cl positions (vide supra) but two different positions for S2 that are effectively separated by ∼0.5 Å (Figure S8). The angles in Table 5 were calculated by replacing O5 of the diamagnetic host (**3**) by Cl. This procedure places the paramagnetic Mo(V) center and S2 approximately at the centroids of their respective disordered positions in **1**[54] (Figure S8). The actual angles between the g-axes and the molecular bonds for species 1 (■) and 2 (●) could differ by as much as 10° from those calculated from the symmetric structure of **3** and given in Table 5. The relationships between the molecular structure of the diamagnetic host (**3**), the magnetic vectors (g_1, g_2, g_3) of species 1 (■) of **1** and the crystallographic (a, b, c*) axes are given in Figure 4.

Table 5. Angles (deg) between the g-Axes and Molecular Bonds for Species 1 (■) and 2 (●)[a]

bond	1.998[b]	1.961[b]	1.944[b]
Mo−O4	10	86	82
Mo−O5 → Cl[c]	78	54	38
Mo−S2	84	37	54

[a] Maximum range between angles for species 1 and 2 is 9°. [b] Average g-magnitudes for species 1 and 2. [c] Cl of **1** is in the O5 position of **3**.

The signals from species 3 and 4 (Δ and ◊, Figure 3) are assigned to the structure of **1** in which O4 is replaced by Cl (Figure S8). Since signals from these two magnetically inequivalent but symmetry-related species were not observable in all three rotational planes (Figure 3), meaningful angles relating the g-axes to the crystal frame and the molecular bonds could not be calculated for species 3 and 4.

Electronic Structure Calculations. *cis,trans*-(L-N_2S_2)-$Mo^{V}OCl$ (1). The calculation of the **g**-tensor of **1** is discussed on the basis of the semiempirical electronic structure calculations at the INDO/S-CIS level as well as on scalar relativistic all electron calculations using the ZORA formalism

Structures. The INDO/S calculations were carried out at the experimental geometries. In the scalar relativistic DFT calculations reasonably good agreement with the experimental structures were achieved for both **1** and **2** with most bond distances being within 5 pm of their experimental values (Figure 6). Slightly larger errors are obtained for the more weakly bound nitrogen donors. While in the case of the axial ligand this might have been attributed to a slight overestimation of the trans effect excerted by the strongly bonding oxo group, the artificial lengthening of the equatorial Mo−N distance is a typical shortcoming of present day density functionals. However, the calculated structures are still very reasonable, and consequently, the DFT property calculations were carried out at the optimized geometries.

(106) Hare, C. R.; Bernal, I.; Gray, H. B. *Inorg. Chem.* **1962**, *1*, 831−835.
(107) Carducci, M. D.; Brown, C.; Solomon, E. I.; Enemark, J. H. *J. Am. Chem. Soc.* **1994**, *116*, 11856−11868.
(108) Inscore, F. E.; McNaughton, R.; Westcott, B.; Helton, M. E.; Jones, R.; Dhawan, I. K.; Enemark, J. H.; Kirk, M. L. *Inorg. Chem.* **1999**, *38*, 1401−1410.

Table 6. Composition of the Highest Valence Orbitals in *cis,trans*-(L-N_2S_2)$Mo^{V}OCl$ (**1**) from ROHF-INDO/S Calculations[a]

energy (eV)	% Mo	% Cl	% S2	% S3	% O	% N6	% N7	% rest	description
−9.82	5.1	1.5	0.7	**55.8**	2.6	0.2	22.0	12.1	$S_{\sigma-ip}$ lone pair
−9.66	**13.2**	2.7	**37.2**	**37.1**	1.7	0.5	3.2	4.4	$S_{\sigma-ip}$ lone pair
−8.83	7.9	5.1	14.8	**67.7**	0.6	0.2	1.9	1.9	$S_{\pi-op}$ lone pair
−8.69	1.6	1.7	**78.0**	14.9	1.1	0.5	0.5	1.8	$S_{\pi-op}$ lone pair
−7.81	***73.9***	*4.8*	*2.4*	***17.5***	*0.2*	*0.4*	*0.0*	*0.8*	***Mo-4d$_{xy}$ (SOMO)***
−1.39	**68.6**	8.1	0.7	0.3	**20.3**	0.7	0.1	1.2	Mo-4d_{xz}
−1.15	**63.8**	1.5	4.7	7.2	**20.7**	0.8	0.7	0.6	Mo-4d_{yz}
−0.68	**65.2**	**11.0**	7.0	1.1	5.2	9.1	0.1	1.5	Mo-4$d_{x^2-y^2}$
0.25	**62.8**	0.4	**16.6**	**15.2**	4.2	0.1	0.1	0.4	Mo-4d_{z^2}/5s
1.02	**63.8**	0.3	5.6	4.5	**11.3**	0.4	**10.1**	4.0	Mo-5s/4d_{z^2}

[a] Contributions greater than 10% are shown in bold font; the SOMO is shown by italic font.

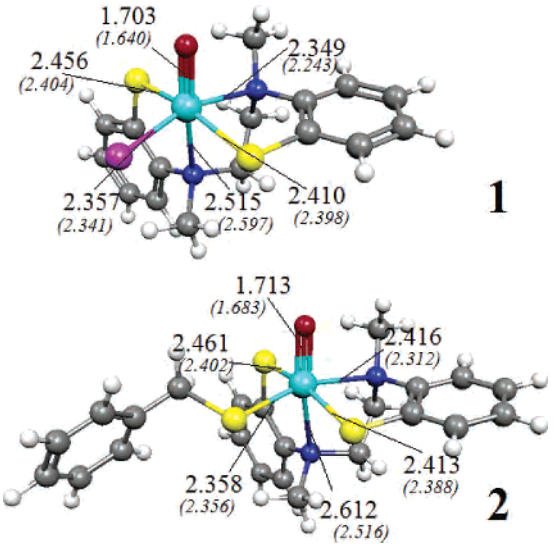

Figure 6. Optimized structures at the BP86/ZORA level with large, uncontracted Gaussian basis sets. Calculated distances are given together with experimental distances (in parentheses).

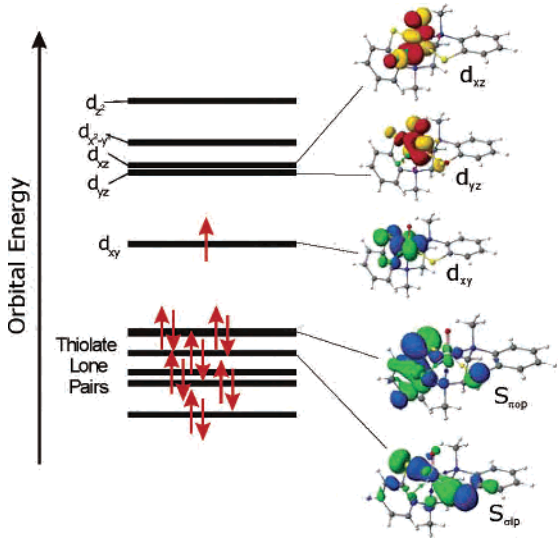

Figure 7. Molecular orbital diagram for **1**. Note that the SOMO is primarily Mo 4d_{xy} and Sπ from S3 (Table 6).

Bonding. The ligand field of **1** is pseudooctahedral with the oxo ligand occupying the $+z$ position in the chosen coordinate system; the two thiolate sulfurs are roughly along the $\pm y$ axes, and the equatorial nitrogen and chlorine donors are roughly oriented along the $\pm x$ axes. In an octahedral ligand field the five Mo 4d orbitals normally split into a triply degenerate t_{2g} and a doubly degenerate higher energy e_g set. Differences in covalencies and donor strengths of the six ligands as well as deviations from perfect octahedral symmetry decrease the effective site symmetry, which results in pronounced orbital splittings within the t_{2g} and e_g sets. The orbital splitting diagram in Figure 7 shows that in both sets of orbitals the splittings are very large and dominated by the oxo ligand, as has been discussed previously by Gray and co-workers[106] and demonstrated by recent MCD and resonance Raman studies.[107−116] The very large π-donor interaction between the central Mo(V) and the oxo-p_x and oxo-p_y orbitals leads to the Mo-d_{xz}- and Mo-d_{yz}-based MOs being ∼2 eV higher in energy than the Mo-d_{xy}-based MO (Figure 7). In addition, strong covalent bonding takes place, as evidenced from ∼20% oxo character mixed into the Mo-$d_{xz,yz}$-based MOs (Table 6). The large destabilization of the Mo-$d_{xz,yz}$-based MOs leaves the Mo-d_{xy}-based MO lowest in energy, and it is the SOMO in **1**. As discussed elsewhere,[117] the cis, trans coordination of the tetradentate L-N_2S_2 ligand results in the two thiolate donors in the equatorial plane being inequivalent, with one of them oriented to have a highly covalent π-bonding interaction with the SOMO. These bonding differences of the two trans S atoms with the SOMO can be clearly seen in the orbital plots in Figure 7 and the breakdown of the MO compositions in Table 6. Therefore, the SOMO carries only ∼75% Mo character (Table 6). This

(109) Note that the energies in Figure 7 are drawn to scale and reflect the zeroth order approximation to the transition energy with the SOMO as the reference MO. Thus, virtual orbital energies reflect the energy of promoting the unpaired electron from the SOMO to the virtual orbital while the energies of the doubly occupied MOs reflect the transition energy from this orbital to the SOMO. This way of plotting orbital energies yields a more intuitively appealing picture than the canonical orbital energies which, in Hartree−Fock and related theories, often leads to SOMO energies that are below some doubly occupied MOs because the canonical MO energies do not properly reflect the electronic relaxation accompanying excitation or ionisation processes and which is very different for metal- and ligand-based MOs.

(110) Zerner, M. C. *Metal-Ligand Interactions: From Atoms, to Clusters, to Surfaces*; Russo, N., Salahub, D. R., Eds.; Kluwer: Dordrecht, The Netherlands, 1992; pp 101−123.
(111) Zerner, M. C. *Metal-Ligand Interactions: Structure and Reactivity*; Russo, N., Salahub, D. R., Eds.; Kluwer: Dordrecht, The Netherlands, 1996; pp 493−531.
(112) Kirk, M. L.; Peariso, K. *Curr. Opin. Chem. Biol.* **2003**, *7*, 220−227.
(113) McNaughton, R. L.; Tipton, A. A.; Rubie, N. D.; Conry, R. R.; Kirk, M. L. *Inorg. Chem.* **2000**, *39*, 5697−5706.
(114) McNaughton, R. L.; Helton, M. E.; Rubie, N. D.; Kirk, M. L. *Inorg. Chem.* **2000**, *39*, 4386-4387.
(115) Helton, M. E.; Kirk, M. L. *Inorg. Chem.* **1999**, *38*, 4384−4385.
(116) McMaster, J.; Carducci, M. D.; Yang, Y.-S.; Solomon, E. I.; Enemark, J. H. *Inorg. Chem.* **2001**, *40*, 687−702.
(117) McNaughton, R. L.; Helton, M. E.; Cosper, M. M.; Enemark, J. H.; Kirk, M. L. *Inorg. Chem.* **2004**, *43*, 1625−1637.

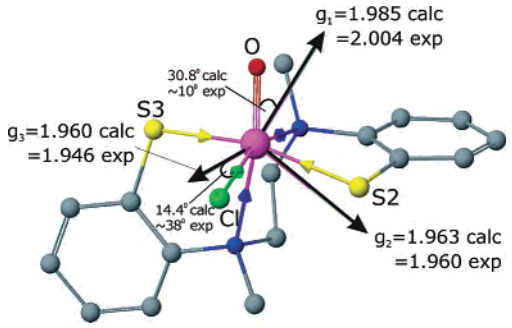

Figure 8. Calculated **g**-tensor orientation for **1** from INDO/S and comparison to experimental values from the single-crystal EPR data.

Table 7. Wiberg Fragment Bond Indices of *cis*,*trans*-(L-N_2S_2)$Mo^{V}OCl$ (**1**) from ROHF-INDO/S Calculations

ligand	Mo	ligand	Mo
Cl	0.708	O	2.362
S2Ph	0.981	N6	0.610
S3Ph	0.968	N7	0.437

number is in excellent agreement with the results of the BP86-ZORA calculation which predicts 76.2%. In the e_g set, the higher Mo-d_{z^2}-based MO is mainly σ-antibonding between the Mo and oxo group while the lower lying Mo-$d_{x^2-y^2}$-based MO is antibonding with the equatorial ligands. The highest energy doubly occupied MOs are mainly comprised of the out-of-plane and in-plane S lone pairs of the equatorial thiophenolate groups of the L-N_2S_2 ligand. The MO compositions obtained in this work are also in very good agreement with the results of DFT computations reported here and previously for a collection of similar complexes.[117] In particular, the shape of the SOMO, which has implications for the electron-transfer properties,[43,117] is quantitatively well reproduced by the present calculations.

The donor strengths of the different ligands are reflected in the Wiberg bond orders collected in Table 7. It is clearly seen that the oxo ligand is by far the strongest donor with a calculated bond order of 2.36 which is excess of a double bond and, in fact, consistent with a formal triple bond between the oxo ligand and the central Mo(V). The calculated bond orders for the two thiolate donors are slightly inequivalent, consistent with the differences in bond lengths observed in the crystal structure[54] and their significantly different orientations relative to the Mo-d_{xy} orbital (Figures 6 and 7). However, both Mo−S bonds are considerably stronger than the Mo−Cl bond. Finally, the two neutral amines are by far the poorest donors in the ligand sphere. Furthermore, the axial amine ligand binds much more weakly to the Mo, which is attributed to the trans effect of the axial oxo group.

Calculated g-Tensor. On the basis of the description of the bonding in **1** presented above, the calculated g-values can be consistently interpreted. First of all, the INDO/S-CI-calculated principal values of the **g**-tensor of $g_1 = 1.985$, $g_2 = 1.963$, and $g_3 = 1.960$ compare reasonably well with the experimental frozen solution values of $g_1 = 2.004$, $g_2 = 1.963$, and $g_3 = 1.946$ (Table 1), which are similar to those determined by single-crystal EPR (Table 4). The main errors in the calculations are the failure to reproduce a positive g-shift for g_1 and the rhombicity in g_2 and g_3 is somewhat smaller than the experimental value. This is different in the scalar-relativistic DFT calculations. At the BP86 level our method predicts principal g-values of 1.950, 1.964, and 2.021, which are in nice agreement with the experimental data, the main error being now a slight overestimation of the positive g-shift. A detailed inspection reveals that the two-electron spin−orbit terms in the mean-field treatment shield about 30−40% of the one-electron contribution which underlines the importance of their explicit inclusion in the treatment.

If we come back to the INDO/S calculations, the calculated orientation of the **g**-tensor is fully consistent with the experimental findings (Figure 8). Thus, the g_1 axis is found to be oriented essentially along the Mo≡O bond, with a deviation of 30.8° degrees compared to ∼10° found experimentally for species 1 and 2 (Table 5). The BP86/ZORA calculations predict an angle of 14.3°, which is in even better agreement with experiment. The axes corresponding to the two smaller g-values are essentially contained in the xy-plane. The g_3 axis is rotated 14.4° (INDO/S) and 3.1° (BP86/ZORA) from the Mo−Cl bond, respectively, compared to ∼38° found experimentally. Finally, the g_2 axis forms an angle of 13.9° (INDO/S) and 17.8° (BP86/ZORA) with the Mo−S2 bond, compared to ∼37° found experimentally. In view of the inherent 5−10° uncertainties in the experimental angles due to the molecular disorder in the crystal (vide supra), there is quite good agreement between theory and experiment concerning both the magnitude and the orientation of the **g**-tensor of **1**, which indicates that the calculations give a reasonably realistic picture of the electronic structure of **1**.

Interpretation of the g-Tensor. It is instructive to analyze the calculated **g**-tensor in terms of the individual contributions from excited states. In our calculations we have taken into account the lowest 119 excited electronic states. However, from this analysis it becomes evident that the two largest g-shifts (g_2 and g_3) are dominated to >90% by the excited states formed from transitions within the Mo-4d manifold. In particular, the g_3 shift is dominated by the Mo-d_{xy} → Mo-d_{yz} transition, which is found in the calculation at 16 400 cm^{-1}. The second largest g-shift is caused by the Mo-d_{xy} → Mo-d_{xz} excited state found at 17 430 cm^{-1} in the calculations. The calculated energies are in good agreement with the suggestion that these transitions occur in the 16 000−18 000 cm^{-1} range, where they are obscured by strong ligand to metal charge-transfer bands.[43,117] If we take C_{4v} as the effective site symmetry, these are the two excited states that are expected from group theory and ligand field theory to give the dominant contributions to the g-shift because they will spin−orbit couple to the $(d_{xy})^1$ ground state. The spin−orbit coupling (SOC) between $(d_{xy})^1$ and $(d_{z^2})^1$ is forbidden due to the SOC selection rule $\Delta m_l \leq 1$ and the fact that the d_{z^2} orbital corresponds to $|m_l| = 0$ and d_{xy} corresponds to $|m_l| = 2$. The transition Mo-d_{xy} → Mo-$d_{x^2-y^2}$ gives rise to SOC in the z-direction and will contribute a negative g-shift. This transition is predicted to occur at 22 000 cm^{-1} (experimentally, the band at ∼18 000 cm^{-1} has been assigned to this transition)[117] and gives a −0.048 contribution to g_1. However, experimentally, this g-shift is found to be small and *positive*. This indicates that there must be canceling

Table 8. Composition of the Highest Valence Orbitals in *cis,trans*-(L-N_2S_2)Mo^{V}O(SCH_2Ph) (**2**) from ROHF-INDO/S Calculations[a]

energy (eV)	% Mo	% SBn[b]	% S2	% S3	% O	% N6	% N7	% rest	description
−9.15	8.2	**74.1**	7.3	3.6	0.2	4.1	1.1	1.4	SCH_2Ph lone pair
−8.85	2.8	**72.3**	7.7	10.3	3.5	1.0	1.6	0.7	SCH_2Ph lone pair
−8.81	8.0	17.8	4.5	**59.4**	1.4	0.1	1.2	7.5	$S_{\pi-op}$ lone pair
−8.58	0.5	**14.0**	**73.8**	**6.5**	1.6	1.6	0.7	1.3	$S_{\pi-op}$ lone pair
−7.57	***75.0***	*4.1*	*2.5*	***16.5***	*0.2*	*0.6*	*0.1*	*1.1*	***Mo-4d$_{xy}$ (SOMO)***
−1.21	**65.0**	3.8	1.8	4.2	**21.5**	3.0	0.1	0.7	Mo-4d$_{xz}$
−1.02	**63.7**	3.0	5.8	2.8	**22.1**	0.7	1.2	0.5	Mo-4d$_{yz}$
0.24	**53.7**	**16.8**	**13.9**	9.1	1.5	4.4	0.1	0.5	Mo-4d$_{x^2-y^2}$
0.59	**63.2**	**10.0**	5.9	9.8	5.9	3.4	0.8	0.9	Mo-4d$_{z^2}$/5s
1.24	**67.3**	4.4	3.5	3.3	**10.2**	0.0	9.3	2.0	Mo-5s/4d$_{z^2}$

[a] Contributions greater than 10% are shown in bold font; the SOMO is shown by italic font. [b] SBn = $^-SCH_2Ph$.

contributions from excited states that are formed from exciting an electron from a doubly occupied MO into the singly occupied MO, since these excited states give positive contributions.[66,67] In fact, in the calculations, we find a large number of LMCT transitions from the equatorial thiolates to the central Mo which start at ∼16 500 cm^{-1} and extend into the far UV region. In particular, the extremely prominent LMCT band observed at 16 000 cm^{-1} is calculated with high intensity ($f \sim 0.07$) at 16 400 cm^{-1} and strongly supports the assignment as S$\pi \rightarrow$ Mo d$_{xy}$.[117] In terms of contributions to the **g**-tensor, no single LMCT excitation makes a dominant positive contribution to the *g*-shift but instead several small contributions add up to a significant positive *g*-shift. However, it is clear that the calculations underestimate the LMCT contribution because the calculated *g*-shift is still negative, whereas the experimental results indicate that the cancellation between the negative d−d and the positive LMCT contributions is almost exact. Qualitatively, the LMCT transitions that can give rise to a positive *g*-shift are those that induce angular momentum in the *z*-direction. This can only happen if the orbitals that are involved are centered on the same fragments as the SOMO. In the present case, the relevant LMCT state must involve a σ-bonding lone pair on S3 because the rotation from a p$_y$ orbital (σ-lone pair) into the Sp$_x$ contribution of S3 to the SOMO will give an angular momentum in the *z*-direction (Figure 7). Hence, this will contribute a positive *g*-shift, which may be significant owing to the SOC constant of sulfur of ∼380 cm^{-1} and the high covalency of the SOMO (∼20% S-character, Table 6 and ref 117). The transition to this state is expected to be weak in absorption and MCD spectra. In fact, experimentally, the transition at ∼21 000 cm^{-1} has been assigned to the S$_\sigma$ → SOMO transition,[117] which shows that a significant contribution to the **g**-tensor from this mechanism is energetically feasible. In the INDO/S-CIS calculations the S$_\sigma$ → SOMO transition distributes over a significant number of final states in the CI procedure, and therefore a clear-cut assignment is not possible. This too-large CI mixing is probably one of the main reasons for the inability of the present calculations to reproduce the small positive *g*-shift observed in **1**.

Hyperfine Couplings. The calculated ^{95}Mo hyperfine couplings predicted by the BP86/ZORA method are in rather moderate agreement with the experimental values. The predicted couplings are 12.0 × 10^{-4}, 12.0 × 10^{-4} (we average over nearly identical perpendicular components in the following), and 37.3 × 10^{-4} cm^{-1} compared to experimental values of 22.3 × 10^{-4}, 23.7 × 10^{-4}, and 58.4 × 10^{-4} cm^{-1}. The contact contribution to the calculated value is +17.8 × 10^{-4} cm^{-1}, and the dipolar and spin−orbit terms contribute (−8.0, +16.0) × 10^{-4} and (+2.2, +3.5) × 10^{-4} cm^{-1} and are therefore limited. Thus, the error in the calculations amounts to ∼20 × 10^{-4} cm^{-1} on all components, which is suggestive that the isotropic Fermi contact-like contribution is the dominant source of error (note that the Fermi contact term in the familiar form does not arise in a genuine relativistic treatment). This is a reasonable suggestion on the basis of the results of refs 118 and 95 which suggest that the core level spin polarization is too low in nonhybrid density functionals. In fact, it is pleasing to observe that the hybrid B3LYP functional predicts an increased contact-like coupling from 17.8 × 10^{-4} to 24.3 × 10^{-4} cm^{-1} which, together with increased dipolar couplings of (−9.3, 18.6) × 10^{-4} cm^{-1} and spin−orbit terms of (2.3, 4.6) × 10^{-4} cm^{-1}, brings the calculated values of 17.3 × 10^{-4} and 47.5 × 10^{-4} cm^{-1} much closer to the experimental values. The remaining error is still largely attributed to the contact contribution which will probably require improved density functionals. An easy remedy would be to increase the amount of Hartree−Fock exchange beyond the 20% contained in B3LYP, but in our opinion this is not a satisfactory procedure. Finally, it is noted that the angle between g_{max} and A_{max} is calculated to be 16.1° in the BP86/ZORA calculations, which is in good agreement with ∼24° found experimentally.[43]

Table 9. Wiberg Fragment Bond Indices of *cis,trans*-(L-N_2S_2)Mo^{V}O(SCH_2Ph) (**2**) from ROHF-INDO/S Calculations

ligand	Mo	ligand	Mo
SCH_2Ph	1.09	O	2.29
S2	0.97	N6	0.57
S3	0.98	N7	0.44

g-Tensor Calculations for *cis,trans*-(L-N_2S_2)Mo^{V}O(SCH_2Ph) (2). On the basis of the good results obtained for **1**, it is reasonable to expect that the semiempirical and DFT calculations also provide a consistent bonding picture for *cis,trans*-(L-N_2S_2)Mo^{V}O(SCH_2Ph) (**2**). The calculations show that the general electronic structure pattern for **2** is extremely similar to that for **1**. The results of the population analysis collected in Tables 6−9 reveal some interesting similarities and differences between the electronic structures of **1** and **2**. The SOMO of **2** is still predominantly Mo-4d$_{xy}$-based, and the unique π-interaction between Mo and S3 is pre-

(118) Munzarova, M.; Kaupp, M. *J. Phys. Chem. A* **1999**, *103*, 9966.

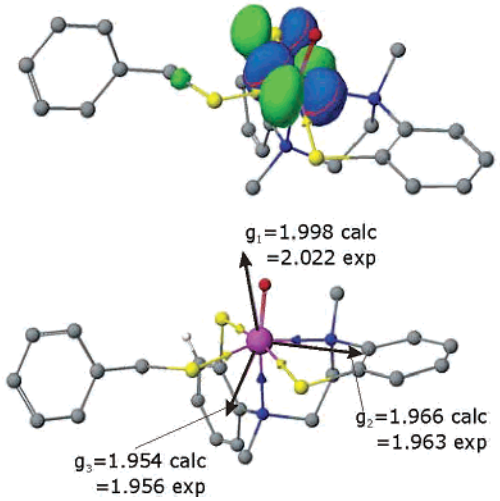

Figure 9. Top: Probability amplitude contours for the calculated SOMO of **2**, showing that the composition of the orbital is similar to that of **1** (Figure 7, Table 6). Bottom: Calculated orientation and magnitudes of the **g**-tensor and comparison of the magnitudes of the individual *g*-values to the experimental values (Table 1).

served; there is rather little spin density picked up by the $^{-}SCH_2Ph$ ligand (~4% by INDO/S (Table 8) and ~3% from BP86/ZORA). These results for **2** are consistent with the MCD, resonance Raman, and theoretical study,[117] as well as with pulsed EPR studies which show only small hyperfine couplings with the methylene protons of the $^{-}SCH_2Ph$ ligand.[119] Nevertheless, the $^{-}SCH_2Ph$ ligand binds more strongly to the central Mo than Cl^{-}, as is evidenced by its increased bond order (1.09 vs. 0.71, Tables 7 and 9). Table 8 shows that both S lone pairs on the $^{-}SCH_2Ph$ ligand are higher in energy than the $S_{\sigma-ip}$ lone pairs of the tetradentate L-N_2S_2 ligand and that one of them (−8.85 eV) is essentially degenerate with the more stable $S_{\pi-op}$ lone pair of L-N_2S_2 (−8.83 eV, Table 6). The monodentate $^{-}SCH_2Ph$ ligand binds more strongly to Mo than do S2 and S3 of the L-N_2S_2 ligand, whose Mo−S bond orders are nearly identical (0.98 and 0.97, respectively, Table 9) and essentially unchanged from those for **1** (Table 7). The Mo≡O and Mo−N6 bonds for **2** are slightly weakened compared to **1**, and these differences are consistent with the orientation of the $^{-}SCH_2Ph$ ligand (Figure 9). The Sπ donor orbital of $^{-}SCH_2Ph$ is approximately parallel to the Mo≡O bond, and thus may compete with the terminal oxo ligand as a π-donor; the σ-bond of $^{-}SCH_2Ph$ is trans to N6.

The calculated **g**-tensor is displayed together with the SOMO in Figure 9. It is seen that the calculated *g*-values agree very nicely with the experimental values and also reproduce the rhombicity in the *x*,*y* plane well (Figure 9). The g_1 axis has the largest *g*-value (smallest *g*-shift), and the g_1 axis is still oriented roughly along the Mo≡O bond with an angle of 29°, similar to the result found experimentally and theoretically for **1**. The values calculated at the BP86/ZORA level are also in nice agreement with experiment and amount to 1.961, 1.975, and 2.035, respectively. The angle between g_1 and the Mo≡O bond is calculated to be 15.6°, again in line with the results on **1.** If A_1 is along the Mo≡O bond, as is typically found for oxo−Mo(V) complexes,[44−46,48−53,107,108] then the calculated orientation for g_1 in **2** is also consistent with the frozen-solution EPR data that give an angle of 24° between g_1 and A_1 (Table 1). As with **1**, the calculated g_1 shift of **2** is somewhat underestimated by INDO/S but is close to experiment in the BP86/ZORA calculations. The axes of the two smaller *g*-values (g_2 and g_3) are aligned largely in the *x*,*y* plane. For **2**, the g_2 and g_3 axes are primarily oriented between the Mo−ligand bonds within the equatorial plane (Figure 9) in either set of calculations, whereas for **1** these *g*-axes are oriented more nearly along the Mo−Cl and Mo−S2 bond vectors (Figure 8). The calculated **g**-tensor orientations for **1** and **2** suggest that subtle changes in the nature and/or orientation of the equatorial ligands of oxo−Mo(V) centers may produce significant changes in the orientation of the **g**-tensor within the equatorial plane even though the changes in the magnitudes of the *g*-values may be relatively small. The calculated ^{95}Mo hyperfine couplings were quite similar to **1** and will not be further discussed.

Implications for Molybdenum Enzymes. The relationships between the EPR signals observed for the Mo(V) states of enzymes and the coordination environment and electronic structure of the Mo center have been of interest since the first enzyme EPR signals were observed in 1959.[120] However, the first crystal structure of a molybdenum enzyme did not appear until 1995,[22] and as yet, no X-ray structure has been determined for an enzyme in the intermediate or transient Mo(V) state that is present during catalysis. Previous EPR studies of Mo(V) compounds have provided considerable insight into the coordination about molybdenum through ligand hyperfine interactions and the observed empirical correlations between the *g*-values and $A(^{95,97}Mo)$ hyperfine interactions for the Mo(V) center.[20,21,33−43] The advent of crystal structures for several molybdenum enzymes,[3,10] especially SO[13] and XO[24,25] which have been extensively studied by EPR spectroscopy under a variety of conditions, has reawakened interest in the synthesis of oxo−Mo(V) compounds with equatorial thiolate ligands that mimic the coordination in these enzymes[37,42,43] and in determining the relationships between the experimental EPR parameters and the structure of the Mo(V) center.[43] Compound **1** (*cis*,*trans*-(L-N_2S_2)$Mo^{V}OCl$) is isomorphous with diamagnetic (*cis*,*trans*-(L-N_2S_2)$Mo^{VI}O_2$) (**3**),[35,54] which enabled large single crystals of **3** doped with **1** to be prepared for single-crystal EPR spectroscopy. Independent molecular orbital calculations on **1** were carried out concurrently with the single-crystal EPR investigation. The good agreement between the theoretical and experimental results for **1** is extremely encouraging and provides a basis for interpreting the EPR spectra of **2** (*cis*,*trans*-(L-N_2S_2)$Mo^{V}O(SCH_2Ph)$), for which it has not yet been possible to synthesize a diamagnetic host. Previous approaches to calculating the EPR parameters of Mo(V) centers have emphasized the importance of covalency, low-energy excited states, and ligand spin−orbit

(119) Astashkin, A. V.; Cosper, M. M.; Raitsimring, A. M.; Enemark, J. H. *Inorg. Chem.* **2000**, *39*, 4989−4992.

(120) Bray, R. C.; Malström, B. G.; Vänngård, T. *Biochem. J.* **1959**, *73*, 193.

coupling.[50,58,59] The computational method used here includes all of these contributions as well as extensive configuration interaction at very low computational expense. Thus, this computational method holds great promise for extension to analysis of the EPR spectra of other analogue systems, to Mo(V) centers in enzymes, and to unstable intermediates. In addition, the present scalar relativistic BP86/ZORA results in combination with accurate multicenter mean-field spin−orbit operators may be among the first of their kind in the sense of combining scalar relativistic SCF/ZORA calculations with spin−orbit coupling perturbation theory for the **g** and metal hyperfine tensors. In this sense, we conclude that the pilot results have been successful and encourage the further development of modern DFT methods for the calculation of EPR parameters in heavier transition metal complexes. (For other applications of EPR parameter calculations to systems containing heavier metals see references 61, 63, 64, and 121.) In particular, this work validates this approach for the case of Mo(V) and we are looking forward to applying this methodology to the calculation of EPR parameters of enzyme intermediates.

Finally, the results presented here for **1** and **2** suggest that the active sites of SO and XO, which have square pyramidal coordination,[9,10,13] have their largest g axis approximately parallel to the Mo≡O bond and roughly perpendicular to the equatorial plane, which contains g_2 and g_3. The orientations and magnitudes of the g_2 and g_3 axes, however, may be subtly dependent upon the nature and conformation of the equatorial ligands. We hope that these results and suggestions will stimulate additional theoretical and single-crystal EPR investigations of low-symmetry oxo−Mo(V) centers in synthetic compounds and molybdenum enzymes.

Acknowledgment. This work is supported by grants from the National Institute of Health (GM 37773 to J.H.E.) and the National Science Foundation (Grant CHE 9610374) for the EPR spectrometer. F.N. acknowledges financial support from the Max Planck Society, the Fonds der Chemischen Industrie, and the DFG within the priority program 1137 "Molecular Magnetism".

Supporting Information Available: Plots of EPR data and tables of crystal data, structure solution, and refinement, atomic coordinates, bond lengths and angles, and anisotropic thermal parameters for *cis,trans*-(L-N_2S_2)MoO_2{O,Cl} (PDF) and crystallographic data in CIF format. This material is available free of charge via the Internet at http://pubs.acs.org.

IC0483850

(121) (a) Patchkovskii, S.; Ziegler, T. *J. Chem. Phys.* **1999**, *111*, 5730. (b) Patchkovskii, S.; Ziegler, T. *J. Phys. Chem.* **2001**, *105*, 54490. (c) Patchkovskii, S.; Ziegler, T. *J. Am. Chem. Soc.* **2000**, *122*, 3506. (d) Arbuznikov, A.; Kaupp, M.; Malkin, V.; Reviakine, R.; Malkina, O. *Phys. Chem. Chem. Phys.* **2002**, *4*, 5467. (e) Frantz, S.; Hartmann, H.; Doslik, N.; Wanner, M.; Kaim, W.; Kümmerer, H.-J.; Denninger, G.; Barra, A.-L.; Duboc-Toia, C.; Fiedler, J.; Ciofini, I.; Urban, C.; Kaupp, M. *J. Am. Chem. Soc.* **2002**, *124*, 10563. (f) Kaupp, M.; Reviakine, R.; Malkina, O.; Arbuznikov, A.; Schimmelpfennig, B.; Malkin, V. *J. Comp. Chem.* **2002**, *23*, 794. (g) Arratia-Perez, R.; Hernandez-Acevedo, L. *J. Chem. Phys.* **2003**, *118*, 7425.